Ionization quenching in scintillators used for dosimetry of mixed particle fields

Christensen, Jeppe Brage; Almhagen, Erik; Stolarczyk, Liliana; Vestergaard, Anne; Bassler, Niels; Andersen, Claus E.

Published in:
Physics in Medicine and Biology

Link to article, DOI:
10.1088/1361-6560/ab12f2

Publication date:
2019

Document Version
Peer reviewed version

Ionization quenching in scintillators used for dosimetry of mixed particle fields

To cite this article before publication: Jeppe Brage Christensen *et al* 2019 *Phys. Med. Biol.* in press https://doi.org/10.1088/1361-6560/ab12f2

Ionization Quenching in Scintillators used for Dosimetry of Mixed Particle Fields

Jeppe Brage Christensen[1], Erik Almhagen[2,3], Liliana Stolarczyk[2,4], Anne Vestergaard[5], Niels Bassler[6,7,8] and Claus E. Andersen[1]

[1]Center for Nuclear Technologies, Technical University of Denmark, Roskilde, Denmark
[2]Skandionkliniken, Uppsala, Sweden
[3]Medical Radiation Sciences, Department of Immunology, Genetics and Pathology, Uppsala University, Uppsala, Sweden
[4]Institute of Nuclear Physics Polish Academy of Sciences in Krakow, The Bronowice Cyclotron Centre, Krakow, Poland
[5]Danish Center for Particle Therapy, Aarhus University Hospital, Aarhus, Denmark
[6]Medical Radiation Physics, Department of Physics, Stockholm University, Stockholm, Sweden
[7]Department of Oncology and Pathology, Medical Radiation Physics, Karolinska Institutet, Stockholm, Sweden
[8]Department of Experimental Clinical Oncology, Aarhus University Hospital, Aarhus, Denmark

jepb@dtu.dk
March 21, 2019

Abstract

Ionization quenching in ion beam dosimetry is often related to the fluence- or dose-averaged linear energy transfer (LET). Both quantities are however averaged over a wide LET range and a mixed field of primary and secondary ions. We propose a novel method to correct the quenched luminescence in scintillators exposed to ion beams. The method uses the energy spectrum of the primaries and accounts for the varying quenched luminescence in heavy, secondary ion tracks through amorphous track structure theory. The new method is assessed against more traditional approaches by correcting the quenched luminescence response from the BCF-12, BCF-60, and 81–0084 plastic scintillators exposed to a 100 MeV pristine proton beam in order to compare the effects of the averaged LET quantities and the secondary ions. Calculations and measurements show that primary protons constitute more than 92 % of the energy deposition but account for more than 95 % of the luminescence signal in the scintilllators. The quenching corrected luminescence signal is in better agreement with the dose measurement when the secondary particles are taken into account. The Birks model provided the overall best quenching corrections, when the quenching corrected signal is adjusted for the number of free model parameters. The quenching parameter kB for the BCF-12 and BCF-60 scintillators is in agreement with literature values and was found to be $kB = (10.6 \pm 0.1) \times 10^{-2}\,\mu\text{m}\,\text{keV}^{-1}$ for the 81–0084 scintillator. Finally, a fluence threshold for the 100 MeV proton beam was calculated to be of the order of $10^{10}\,\text{cm}^{-2}$, corresponding to 110 Gy, above which the quenching increases non-linearly and the Birks model no longer is applicable.

Keywords: Organic plastic scintillators; particle dosimetry; ionization quenching; proton therapy

1 Introduction

Organic plastic scintillators are attractive for particle dosimetry due to a prompt signal, good water equivalence, and a small volume (Beddar et al., 1992a,b). Nonetheless, the luminescence signal deviates from the dose deposition along the beam axis, an under response termed ionization quenching, as the linear energy transfer (LET) increases. Several methods have been suggested to correct the ionization quenching in solid state detectors: A semi-empirical formula due to Birks (1951) has historically been successfully applied to correct the ionization quenching in scintillators, although the model requires a priori knowledge about the quenched response and is incapable of predicting the quenching. Murray and Meyer (1961) demonstrated a shortcoming for the model for ions, while Boivin et al. (2016) recently showed how the model breaks down for low-energy photons. The Birks model was extended by Chou (1952) with an additional quenching parameter with mixed success; Birks (1964) examined the Chou model and found the best fit when the additional parameter vanished, thereby reducing it to the Birks model. That is in contrast to Torrisi (2000) who obtained a better agreement between the model and data when the additional parameter is included. However, neither the Chou nor Birks model accounts for the radial energy

deposition by secondary electrons (EDSE), which requires the model parameters to be experimentally determined for each primary ion and scintillator while the luminescence from heavier, secondary ions is omitted. Furthermore, the models cannot account for the temporal structure of quenching.

Blanc et al. (1962, 1964) proposed a kinematic quenching model relying on the light yield and decay time of the scintillator, which can be simplified to the Birks model (Birks, 1964) without the temporal component. The model allows excited states (excitons) to diffuse, fluorescence, and quench which enables a calculation of the quenching as well as quantifying the temporal structure of the quenched luminescence signal. The Blanc model has been implemented in the open-source software `ExcitonQuenching` (Christensen and Andersen, 2018) which applies amorphous track structure theory to distribute the initial exciton density in an ion track. Amorphous track structure theory models, in contrast to a stochastic track structure theory, the radial energy deposition with a continuous penumbral region and a dense core region depending on the kinetic energy and LET of the given ion. `ExcitonQuenching` is consequently able to calculate the temporal structure of quenching as well as distinguishing between the quenching in ions with different atomic number through track structure theory, unlike the Birks and Chou models.

Secondary protons and heavier ions in a clinical proton beam constitute as much as 8 % of the total dose (Paganetti, 2002). The LET contribution from secondary protons gives rise to an elevated LET which can have an impact on the the relative biological effectiveness (RBE) (Grassberger and Paganetti, 2011). The situation is reversed in scintillator dosimetry, where the high-LET secondary particles quench the luminescence more than the primary protons. Grzanka et al. (2018) recently investigated the LET distribution in a spread out Bragg peak in a proton beam with a distinction between the LET from primary protons and all primaries calculated in terms of the fluence-averaged LET (LET_Φ) and dose-averaged LET (LET_D). The distinction between the primaries and all particles gave as much as ≈ 300 % LET differences and highlights the importance of LET calculations for quenching corrections. The LET_D was recently shown to be a questionable predictor for the RBE (Grün et al., 2018), as the LET_D poorly resembles a broad LET distribution, which similarly would give rise to a biased quenching correction in scintillator dosimetry. This motivates an investigation of how the averaging of the mixed particle field and the LET spectrum affects the quenching corrections in ion beams.

The present work applies the `ExcitonQuenching`, Birks, and Chou models to correct the ionization quenching in three organic plastic scintillators exposed to a pristine proton beam where the primary particles and nuclear fragments are taken into account. We assess how the LET-averaging affects the quenching corrections relative to the use of the entire LET spectrum and secondary ions. Furthermore, the traditional quenching correction methods rely on the implicit assumption that ionization quenching in ion tracks are independent events; such a presumption is assessed with `ExcitonQuenching`, where the temporal and spatial components enable an estimation of a fluence threshold, above which the excitons in ion tracks will interact on average and increase the ionization quenching.

2 Materials and Methods

2.1 Experimental setup

Three organic, plastic scintillators (BCF-12 and BCF-60, Saint-Gobain, France; 81-0084, Industrial Fiber Optics, Inc, USA) with a diameter of 1 mm and 2 mm length were coupled to optical fibers connected to the ME-40 data acquisition system (Andersen, 2011). The scintillators were irradiated in a water phantom with 100 MeV protons in a spot-scanned beam at the Skandion Clinic, Uppsala, Sweden. The primary proton fluence was estimated to be $\Phi = D/s = 5.5 \times 10^8$ cm^{-2} from a dose measurement $D = 0.635$ Gy at 2 mm water depth with an electronic mass stopping power $s = 7.25$ MeV cm^2 g^{-1} at 100 MeV.

A reference depth-dose curve of the 100 MeV protons in the water phantom was measured with an ionization chamber (Roos, PTW Freiburg GmbH, Germany) which is used to validate the Monte Carlo model of the experimental setup. Two scintillators are introduced at a time in a hollow acrylic (PMMA) cylinder, see figure 2.1, carved to match the outer diameter of the ionization chamber in order to fit the same holder in the water phantom. The response curve of each scintillator in the water phantom was measured twice. The detector response from the water surface to 6.9 cm water depth was measured with 3 mm and 1 cm steps for the ionization chamber and scintillators, respectively. Both step sizes were 0.3 mm onwards.

2.1.1 Monte Carlo scoring of the dose and LET

A model of the experimental setup is implemented in `Geant4` (Agostinelli et al., 2003) version 10.4.p02 using the `QGSP_INCLXX_EMZ` physics list. A beam model detailed in Almhagen et al. (2018) was used, which was validated against measured dose distributions and thus has a demonstrated ability to recreate the nuclear halo. The `Geant4`

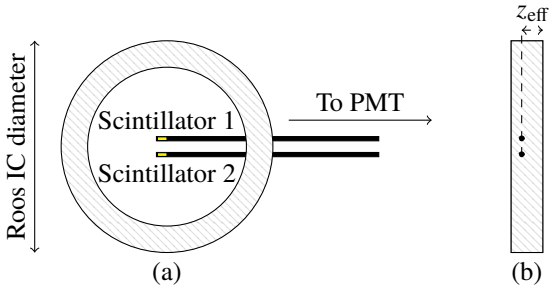

Figure 2.1: (a) The PMMA ring with an outer diameter matching the Roos chamber holder with the fiber-coupled scintillators connected to a photomultiplier tube (PMT). (b) Side view of the ring where the two holes are drilled at a distance z_{eff} corresponding to the effective point of measurement of the ionization chamber.

model enables a scoring of the energy deposition and LET spectra for both primary and secondary particles at any point in the scintillator and ionization chamber during the experiments.

The LET is scored in `Geant4` as both LET_Φ and LET_D following the recommended definition in Cortés-Giraldo and Carabe (2015), where the LET in the latter case is extracted from the `Geant4` electronic stopping power tables. The dose and LET quantities are scored in voxels of side length 1 mm. The LET values in the tables and figures below are given as the LET in water. The stopping power ratios between water and the scintillating material in question are used to estimate the LET in the scintillator for quenching calculations.

The active volume in a scintillator causes an averaging of the sharp dose gradients at the pristine Bragg peak. The volume averaging is assessed through a Monte Carlo approach by scoring the dose and LET in cylinders placed along the beam axis with the cylinder axis perpendicular to the beam direction for different radii.

2.2 Quenching corrections

2.2.1 Semi-empirical quenching corrections

The luminescence $\mathrm{d}L$ per unit length $\mathrm{d}x$ of an ion incident on a scintillator with light yield per energy A will in the absence of ionization quenching equal the number of photons emitted per deposited energy, i.e. $N \equiv A \cdot \text{LET}$. However, the luminescence is reduced with the quenching correction factor (QCF) as

$$\frac{\mathrm{d}L}{\mathrm{d}x} = A\,\frac{\text{LET}}{\text{QCF}}, \qquad \text{for} \quad 1 \leq \text{QCF} = 1 + kB \cdot \text{LET} + C \cdot \text{LET}^2 + \cdots, \tag{2.1}$$

where kB and C are model parameters to be determined experimentally. The case $C = 0$ reduces eq. (2.1) to the Birks model (Birks, 1951) and $C \neq 0$ corresponds to the second-order model due to Chou (1952), which both typically rely on the LET_Φ.

2.2.2 Theoretical quenching corrections

Amorphous track structure models have historically been successfully applied to model the radial energy distribution. This work relies on the track structure model due to Scholz and Kraft (1996), as outlined in appendix A.1, to model the radial exciton density in ion tracks.

The exciton density $n(r,t)$ in an ion track is at $t = 0$ governed by the amorphous track structure model and changes in time and space according to the kinematic Blanc model (Blanc et al., 1962, 1964)

$$\frac{\partial n}{\partial t} = D\nabla^2 n - \tau^{-1} n - \alpha n^2, \tag{2.2}$$

where D is the exciton diffusion constant, $\tau^{-1} = p + k$ is the decay time of the scintillator, and p, k, and α are the rate of fluorescence emission, uni-, and bimolecular quenching parameters, respectively. The solution to eq. (2.2), subject to the initial condition given by the amorphous track structure model for a given ion and scintillator, is implemented in the open-source repository `ExcitonQuenching`[1]. The scintillator parameters τ and A are listed in table 1 whereas the Blanc model parameters are given in Christensen and Andersen (2018) along with a detailed

[1] Available for download at `https://github.com/jbrage/ExcitonQuenching`

model explanation. The light emission from the scintillator caused by an incident ion is calculated by integrating over the fluorescence term in eq. (2.2), and the QCF is subsequently computed as the ratio of the light emission excluding quenching (i.e. with $\alpha = 0$) to the light emission including quenching ($\alpha \neq 0$).

2.2.3 Quenching corrections in a mixed radiation field

A primary or secondary ion i depositing a dose $D_i(x)$ at the depth x will in a quenching-free case for QCF $\simeq 1$ give rise to a fraction $w_i(x) = D_i(x)/D_{\text{total}}(x)$ of the luminescence signal, where $D_{\text{total}}(x)$ denotes the total dose at the given depth. Nonetheless, when quenching is present, the light output for the ion i is reduced with a factor $\text{QCF}_i > 1$, corresponding to a quenched luminescence signal as $w_i(x)/\text{QCF}_i(x) < 1$. Consequently, a common correction factor $\text{QCF}_{\text{total}}$ for the total quenched luminescence signal is computed as

$$\frac{1}{\text{QCF}_{\text{total}}(x)} = \frac{1}{D_{\text{total}}(x)} \sum_i \frac{D_i(x)}{\text{QCF}_i(x)}, \tag{2.3}$$

where the summation runs over primary and secondary protons ions, deuterons, tritons, and two isotopes of helium. The Birks and Chou models are not directly applicable when eq. (2.3) is inserted into eq. (2.1) as the quenching parameters for both models vary for each type of ion and require experimental determinations. Thus, only `ExcitonQuenching` is applied as it accounts for the varying radial energy deposition through amorphous track structure theory. The `ExcitonQuenching` calculation of ionization quenching in ion tracks with atomic number $z \leq 6$ was validated in Christensen and Andersen (2019).

2.2.4 Comparison of quenching models

The quenching corrections for the three organic plastic scintillators are calculated with five approaches:

(A) With `ExcitonQuenching` for the case where only the luminescence from primary protons is considered, and the LET_Φ for primary protons is used to correct the quenching.

(B) Using `ExcitonQuenching` where the quenching from both primary and secondary ions are taken into account and the quenched signal is corrected with a common correction factor according to eq. (2.3).

(C) By fitting the linear Birks model to the experimentally determined QCFs as a function of LET_Φ for primaries and secondary protons in line with other studies (Wang et al., 2012; Hoehr et al., 2018).

(D) By fitting the second-order Chou model to the QCFs as a function of LET_Φ for primaries and secondary protons directly in eq. (2.1).

(E) With a convolution of the the Chou model and the proton LET spectrum, which gives a quenching correction factor as a function of depth as

$$\text{QCF}(x) = 1 + kB \cdot \text{LET}_\Phi(x) + C\left(\text{LET}_\Phi{}^2(x) + \sigma^2(x)\right),$$

as derived in appendix A.2. I.e., the second-order term in Chou model is no longer a function of the fluence-averaged LET in eq. (2.1) alone but perturbed by the variance of the LET spectrum.

Goodness of fit The quality of the quenching corrected scintillator signal S_{scint} with variance σ^2_{scint}, compared to the dose distribution measured with an ionization chamber S_{IC}, is evaluated through the χ^2 per degree of freedom (dof) as

$$\chi^2 = \sum_{i=0}^{n} \frac{(S_{\text{IC},i} - S_{\text{scint},i})^2}{\sigma^2_{\text{scint},i}}, \tag{2.4}$$

where the sum runs over all data points n in the scintillator measurement and the dof is given as n minus the number of model parameters.

2.2.5 Exciton interactions between ion tracks

Overlapping ion tracks is a well-known phenomenon in dosimetry where e.g. initial and general recombination in gas-filled ionization chambers exposed to ion beams requires different correction methods and has previously been investigated numerically (Christensen et al., 2016). The situation is similar in scintillators, although the higher material density and rapid decay time of organic plastic scintillators limits the track interactions. The five quenching corrections in section 2.2.4 all rely on the implicit assumption that the quenching in ion tracks are independent of each other. `ExcitonQuenching` enables a zeroth-order approximation of a fluence threshold where the ion tracks

will overlap on average and increase the quenching non-linearly, and limit the applicability of the Birks and Chou models.

3 Results

3.1 Model and LET spectrum verification

The dose measured with the ionization chamber is compared to the `Geant4` results in figure 3.1, where the dose distributions have not been subject to a peak match. The LET is scored from the entrance to the 80 % distal dose point (Bortfeld, 1997) as illustrated in the figure with a vertical dashed line. The lower figure shows the ratio of the simulated to the measured dose where the discrepancy is less than 2 %. Two measurements of the BCF-12 scintillator are normalized to the entrance and indicate the ionization quenched response relative to the dose measurements as well as alignment errors, which both are to be corrected.

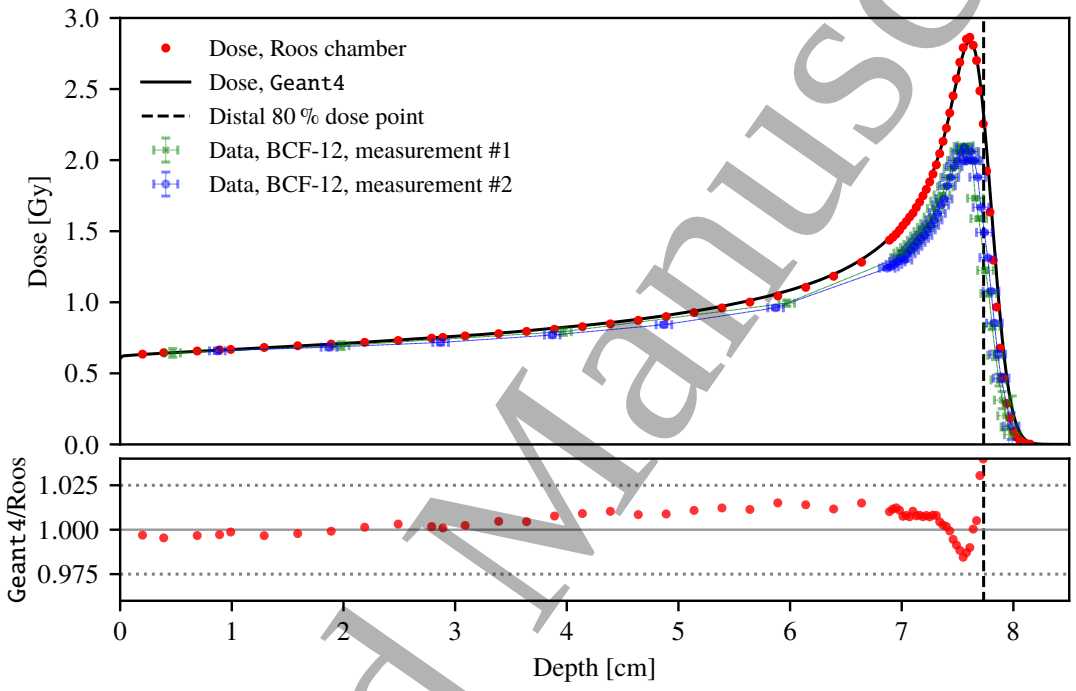

Figure 3.1: Comparison of the dose measured with an ionization chamber (dots) and scored in the `Geant4` model (solid line) in the water phantom. The ratio between the simulated and measured dose is shown below. The 80 % distal dose threshold is delineated with a vertical, dashed line. The two measurements with the BCF-12 scintillators are shown with $k = 2$ statistical uncertainties for reference .

The LET spectrum for both primary and secondary protons are shown in figure 3.2(a). The LET_Φ as a function of depth, corresponding to the arithmetic mean of the spectrum, is shown with a white, dashed line. The LET spectrum at the entry channel is sharply defined but gradually smeared out as the primary protons undergo scattering processes in the water. Figure 3.2(b) shows the LET spectrum extracted at three depths from figure 3.2(a), where the tail contributions from secondary protons are clearly visible at the two shallower depths whereas the LET spectrum at the Bragg peak is wide.

The `Geant4` simulated dose and LET contributions from several ions during the experiments are presented in figure 3.3. Figure 3.3(a) shows the LET_Φ and LET_D from primary and secondary protons along with deuterons, tritons, ^{3}He, and alpha particles with their contributions to the total dose in figure 3.3(b). Although secondary protons only constitute up to 8 % of the total dose, the LET for secondary protons at the entry channel is several times larger than that of the primaries. Isotopes of helium contribute around 0.3 % of the total dose but with elevated LET of more than two orders of magnitude at the entry channel. The total contribution to the dose from secondary ions thus amounts to several percent throughout the beam with an uneven LET distribution, giving rise to a non-linear common quenching correction as a function of depth.

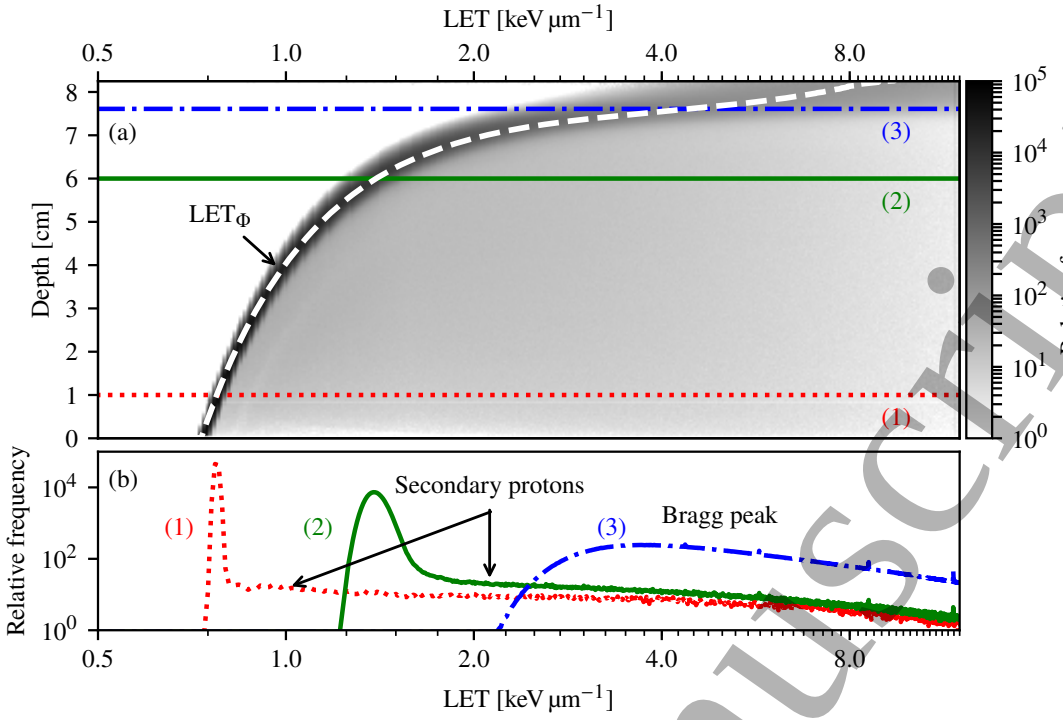

Figure 3.2: (a) `Geant4` calculations of the LET spectrum for primary and secondary protons. The arithmetic mean, the LET$_\Phi$, is delineated with a dashed, white line. The LET distributions at the three depths (1) 1 cm (dotted line), (2) 6 cm (solid line), and (3) the Bragg peak at 7.61 cm (dot-dashed line) are shown in (b). The mean and 1 standard deviation for the three non-normal distributions are (1) (0.780 ± 0.058) keV µm^{-1}, (2) (1.48 ± 0.42) keV µm^{-1}, and (3) (6.07 ± 2.90) keV µm^{-1}.

3.2 Scintillation response

The scintillator response as a function of depth varies from the ionization chamber measurement not only due to ionization quenching but is furthermore subject to both an alignment offset with the ionization chamber as well as a volume averaged signal.

Volume averaging The effect of volume averaging of the dose and LET distributions is investigated in appendix A.3, where the dose and LET$_\Phi$ are scored in 0.1 mm, 1 mm, and 3 mm volumes in `Geant4`. The deviation between the dose and LET$_\Phi$ scored in 1 mm wide voxels to the same quantities scored in 0.1 mm wide voxels is less than 2 % and as such in agreement with the results in Archambault et al. (2008). The 2 % deviation for the 1 mm diameter scintillators is within the experimental uncertainties at the Bragg peak.

Scintillator alignment errors The positioning of the scintillators in the holder is corrected for any misalignment in line with the approach suggested in Wang et al. (2012): The QCFs are for a given depth shift of the scintillator measurement calculated as the ratio between the measured dose and the quenched scintillator signal. The linear Birks model is then fitted to the data as a function of LET$_\Phi$ and the quality of the particular shift is evaluated through χ^2/dof between the model and the experimentally determined QCFs. The best fit is found by interpolation as the shift minimizing χ^2/dof.

A similar approach was applied for method (D) with the Chou model, where the χ^2/dof was calculated after fitting a second-order function to the QCFs, to avoid comparing the quality of the quadratic Chou model to data shifted according to the linear Birks model. The scintillator shift corrections obtained for the Chou model in method (D) were applied to method (E) in order to compare the LET$_\Phi$ and spectrum corrected quenched luminescence. All scintillator measurements were shift corrected less than 1 mm, and the two measurements for each scintillator were subsequently concatenated into a single scintillator response curve.

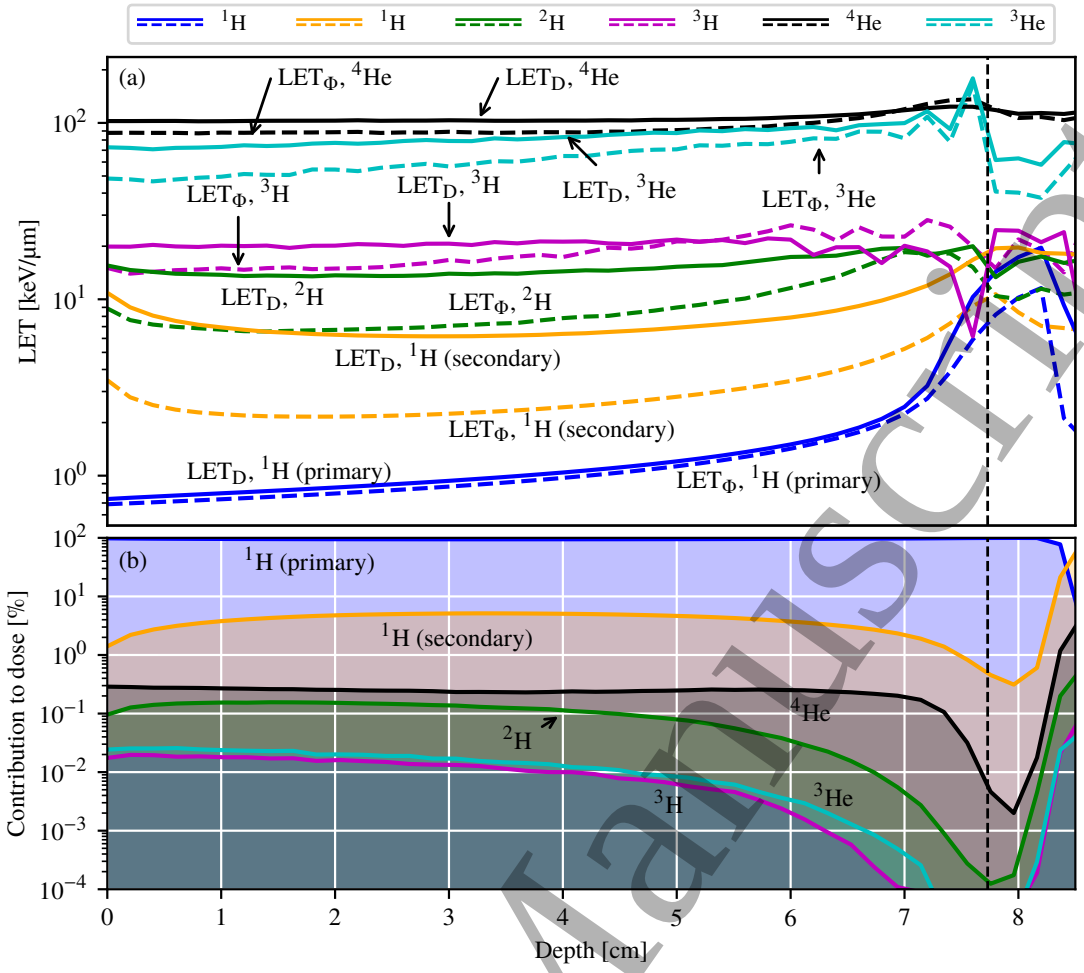

Figure 3.3: (a) LET distributions for primary and secondary protons, deuterons, tritons, ^{3}He, and alpha particles. The LET$_\Phi$ is plotted with dashed lines and the LET$_D$ with solid lines. (b) The dose distributions of the six ions contributing the most to the dose deposition. The dashed vertical lines indicates the distal 80 % dose threshold.

3.3 Quenching corrections models

The experimentally determined QCFs as a function of LET$_\Phi$ for the BCF-12 scintillator are shown in figure 3.4, where the data were shifted according to the Birks model. The QCFs are calculated with `ExcitonQuenching` using methods (A), where only the LET$_\Phi$ from the primary protons in figure 3.2 is taking into account, and (B) which includes the six ions in figure 3.3 and calculates a common QCF as given by eq. (2.3). Method (C) with the Birks model is fitted to the experimentally obtained QCFs with quenching parameter kB listed in table 1. The agreement between the models in figure 3.3 is representative for the results obtained for the BCF-60 and 81–81004 scintillators.

Mixed field quenching The dose-weighted QCF$_{\text{total}}$ for the relevant ions are calculated with `ExcitonQuenching` in approach (B) for the BCF-12 scintillator in figure 3.5. Secondary protons contribute 5 % of the luminescence signal at 3 cm depth although the dose contribution is 8 %, while the primary protons give rise to 95.4 % to 99.8 % of the luminescence signal along the central beam axis. Constant quenching corrections along the beam axis, as the case approximately is for the alpha particles, are negligible for relative scintillator measurements.

Quenching corrections Each of the three quenched scintillator responses is corrected with the five quenching correction methods (A)–(E) and compared to the ionization chamber measurement resulting in the χ^2/dof values listed in table 1. The quenching corrected luminescence signal is compared to the dose measurement in figure 3.6 for methods (A), (C), and (E), where the corrected signals using methods (B) and (D) are omitted for the sake of clarity.

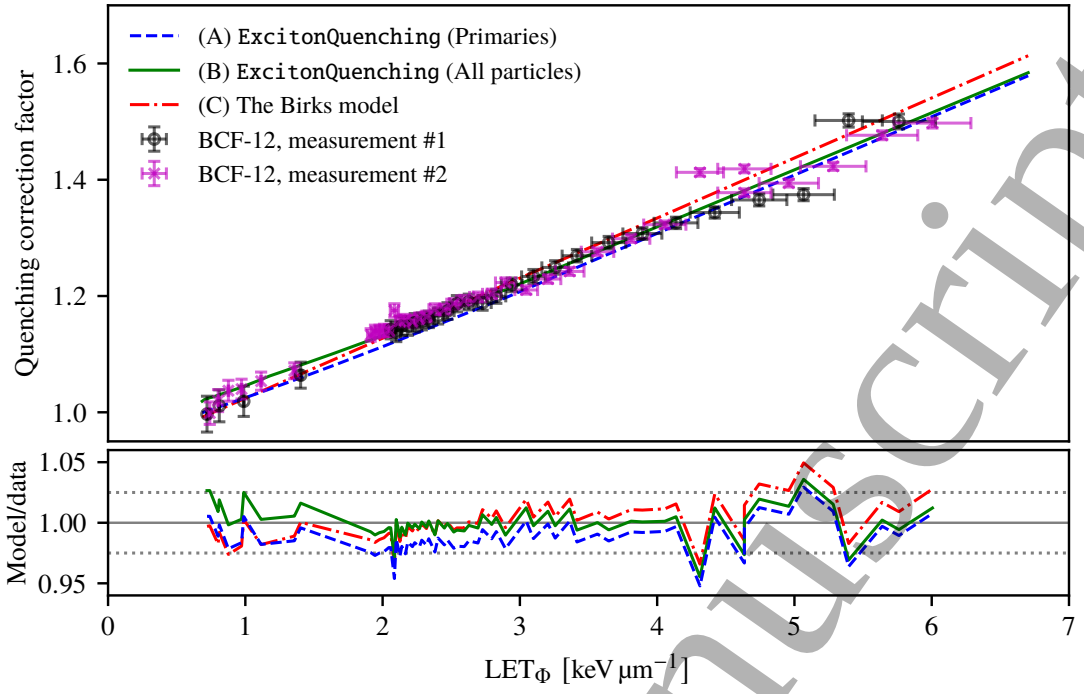

Figure 3.4: The experimentally obtained QCFs for the two BCF-12 measurements where the linear Birks model is fitted to the data. The QCFs are computed with `ExcitonQuenching` using methods (A) and (B). The ratios between the model-predicted to the experimentally determined QCF is shown below with the same line styles as given in the legend above.

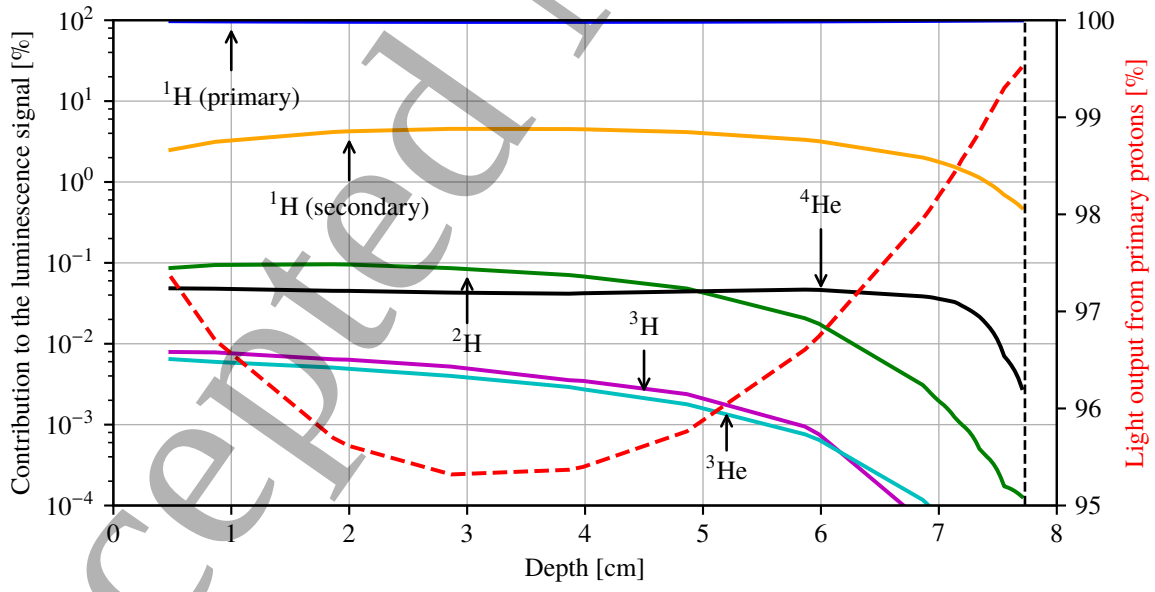

Figure 3.5: The percentage of the total luminescence signal for each of the included ions (solid lines) plotted on the left ordinate as predicted by eq. (2.3) for the BCF-12 scintillator. The right ordinate shows the percentage of the luminescence signal caused by primary protons plotted with a dashed line. The distal 80 % dose point is marked with a vertical, dashed line.

The discrepancies between the corrected scintillator signals and the dose measurement exhibit similar structures. The deviations from the dose measurements are for the entry channel around 2.5 % for the BCF-scintillators and less than 1 % for the 81-0084 scintillator. The deviation at the Bragg peak is for the BCF-12 scintillator within 5 % except for an outlier, whereas the BCF-60 and 81-0084 scintillators both exhibit discrepancies as much as 10 %.

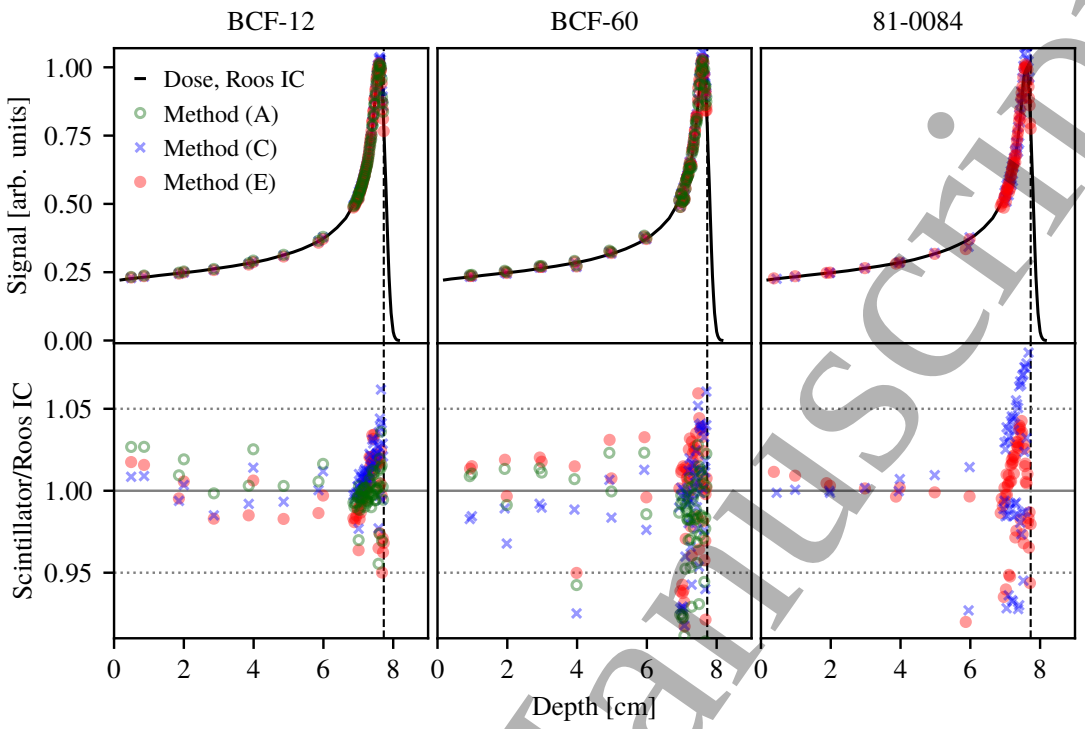

Figure 3.6: The quenched scintillator signal corrected with method (A), where `ExcitonQuenching` relies on the primary protons shown with open circles, method (C) with the Birks model plotted with crosses, and (E) the Chou model, shown with circles, taking the full proton spectrum into account. The ionization chamber measurement is plotted with a solid line. The lower figures show the ratio between each quenching corrected scintillator signal to the ionization chamber measurement where the dotted horizontal lines denote 5 % discrepancies. The χ^2/dof for each method is given in table 1.

Table 1: Comparison of quenching corrected scintillator measurements through χ^2/dof for the five methods (A)–(E). The light yield and decay time for the BCF scintillators are given by the manufacturer (Saint-Gobain, France). The fitted Birks and Chou quenching parameters kB and C in eq. (2.1) are listed for the three scintillators for methods (C) and (D) with ($k = 2$) uncertainties. The quenching parameters are not included for method (E) as it is not a function of LET_Φ alone.

	Methods (A) and (B), `ExcitonQuenching`				Method (C), Birks	
Scintillator	Light Yield [% Anthracene]	τ [ns]	χ^2/dof (A) primaries	χ^2/dof (B) all	kB [µm keV^{-1}]	χ^2/dof
BCF-12	46	3.2	0.72	0.70	0.107 ± 0.003	0.66
BCF-60	41	7.1	1.33	1.26	0.103 ± 0.004	1.12
81-0084[†]	—	—	—	—	0.106 ± 0.001	0.26

	Method (D), Chou (LET_Φ)			Method (E), Chou (LET-spectrum)
Scintillator	C [µm^2 keV^{-2}]	kB [µm keV^{-1}]	χ^2/dof	χ^2/dof
BCF-12	0.007 ± 0.002	0.056 ± 0.009	1.08	1.01
BCF-60	0.004 ± 0.003	0.078 ± 0.010	1.21	1.20
81-0084	0	0.106 ± 0.001	0.27	0.27

[†] The light yield was unavailable and `ExcitonQuenching` as such not applicable.

3.4 Quenching thresholds

The quenching fluence threshold is computed by sampling ion tracks to resemble different fluences. The quenching between two parallel 100 MeV proton tracks in the BCF-12 scintillator is investigated in figure 3.7, where the spatial distance between the two tracks is shown on the abscissa, and the ordinate shows the time between the two protons. The QCF map is calculated by interpolating the QCF results of 5000 uniformly log-sampled points where only a fraction of the samples is shown in the figure. The fluence is approximated as the inverse of the square of the distance between the proton tracks. The QCF = 1.056 for a single ion track for the given proton energy and scintillator, and such a value in the QCF map corresponds to the case, where the quenching in the ion tracks are independent of each other. The horizontal, dashed line in the figure is the characteristic decay time of the scintillator, whereas the dashed, vertical line is the distance corresponding to twice the ion core radius in the Scholz-Kraft model in appendix A.1.

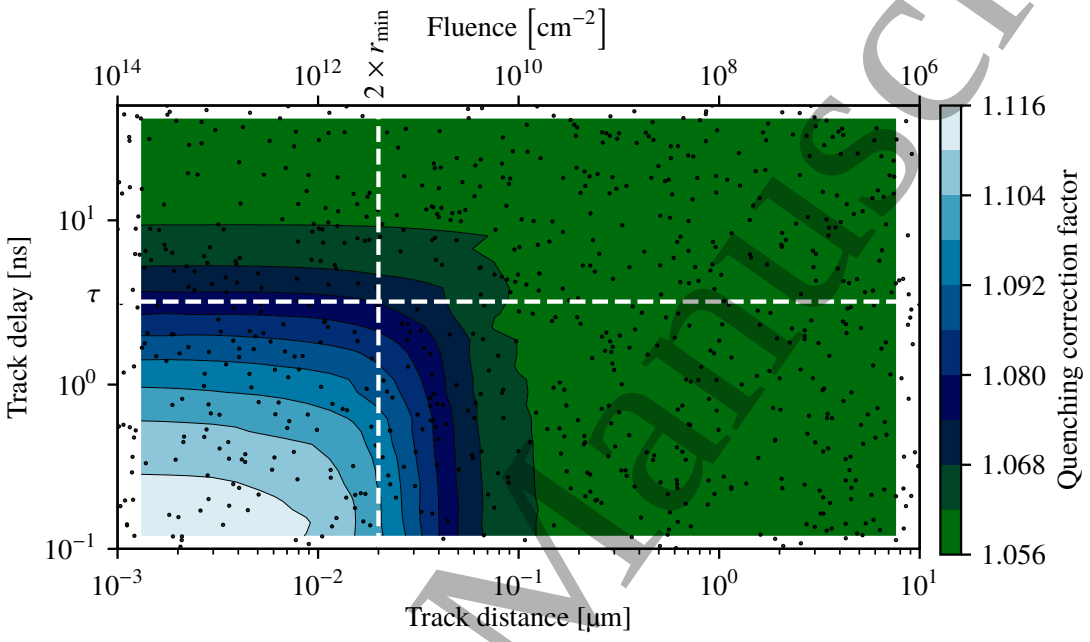

Figure 3.7: The QCF map for two 100 MeV proton tracks computed with `ExcitonQuenching` in the BCF-12 scintillator. The spatial distance between the two ion track centres is shown on the abscissa and the time between the two ions on the ordinate. The horizontal dashed line corresponds to the characteristic decay time of the scintillator τ whereas the vertical dashed line is twice the ion core radius $r_{\min}$.

4 Discussion

4.1 Monte Carlo calculations

`Geant4` model validation The agreement between the `Geant4` calculated dose and the ionization chamber measurements in figure 3.1 confirms the application of the `Geant4` model to calculate the LET and dose distributions in figures 3.2 and 3.3. Furthermore, the dose and LET scoring variations due to volume averaging in appendix A.3 are not corrected as the LET variations are below 2 %, i.e. well below the experimental uncertainties.

Proton LET spectrum The LET spectrum of primary and secondary protons in figure 3.2(a) exhibits a relative sharp fluence distribution at the entry channel as exemplified in figure 3.2(b) at the three depths. As the LET spectrum is sharp at the entry channel $\mathrm{LET}_\Phi{}^2 + \sigma^2 \approx \mathrm{LET}_\Phi{}^2$, i.e. eq. (A.3b) reduces to the normal Chou model as a function of LET_Φ in eq. (2.1) without the variance dependency. As such, the convolution of the Chou model and the LET spectrum in eq. (A.3b) is redundant. The situation differs at the Bragg peak where $\mathrm{LET}_\Phi{}^2/\sigma^2 \simeq 4.4$ and the error on the second-order term in eq. (A.3b) increases correspondingly if the variance of the LET spectrum

is omitted. This shows, that the LET spectrum cannot be neglected at the Bragg peak for the Chou model, which is similar to the $\mathrm{LET_D}$ discussions and conclusion in Grün et al. (2018).

4.2 Scintillator quenching

Quenching correction factors The experimentally determined QCFs in figure 3.4 deviates ±3 % below 4 keV µm^{-1} for methods (A), (B), and (C) except for an outlier. The quenching correction parameter kB in table 1 for the BCF-12 scintillator deviates 10 % and 3 % from the results published in Wang et al. (2012) and Alsanea et al. (2018), respectively. The kB value for the BCF-60 scintillator is between the two values reported by Hoehr et al. (2018). The Chou model in method (D) provided the best fit to the data for $C \neq 0$ for the BCF scintillators, in agreement with Torrisi (2000), and $C = 0$ for the 81–0084 scintillator in agreement with Birks (1964). The quenching parameters kB and C were not extracted for method (E) since the QCFs are obtained as a function of depth rather than $\mathrm{LET_\Phi}$ as the latter is perturbed by the variance of the LET spectrum.

Energy deposition by secondary, heavy ions The contributions from deuterons, tritons, and helium isotopes constitute around 0.3 % of the total dose, except for the dip at the Bragg peak with LETs ranging from 1 to 2 orders of magnitude larger than that of the primaries. The huge LETs combined with slow velocities lead to dense track structures with an enormous local energy deposition and thus ionization quenching. Consequently, the particles heavier than a proton will due to a low dose contribution give rise to a negligible quenching correction in proton beams as shown in figure 3.5 and eq. (2.3). For relative measurements, the inclusion of the heavy secondary ions is negligible, as they contribute almost uniformly to the dose along the beam axis. However, if the light yield of the scintillator is to be calculated from the scintillator measurements as in Alsanea et al. (2018), the quenched light emission from secondary protons needs to be considered and corrected, while the heavier secondary ions would give rise to less than a 1 % luminescence correction. The situation is however different in heavy ion beams where the dose contribution from secondary, heavy ions is significantly larger and needs to be corrected. However, the elevated LET in the plateau region of a heavy ion beam would reduce the experimental uncertainties inevitable related to measurements at the Bragg peak in a proton beam, and thus improve the possibilities for relating ionization quenching to LET and track structure theory.

The dose contribution from secondary protons is uneven and constitutes up to 8 % of the total dose while the LET at the entry channel is comparable to the LET of the primaries at the Bragg peak. Thus, the secondary protons contribute unevenly to the quenching along the beam axis, which is reflected in the better fit for `ExcitonQuenching` method (B) than (A) in table 1, where the former method corrects the quenched signal from all particles.

Quenching models The quenching corrected signals in figure 3.6 all exhibit a similar structure with a deviation around 2 % from the entrance region to 6 cm depth with an increasing discrepancy to 5 % for the BCF-12 scintillator and 9 % for the BCF-60 and 81–0084 scintillators. The Birks model in method (C) gave the overall lowest χ^2/dof in table 1. A direct χ^2/dof comparison across the methods is however difficult as the data for the Birks and Chou models were shifted differently. The Birks model method (C) performs well for quenching corrections in proton beams due to its linearity; The convolution of the LET spectrum and the linear model yields exactly the $\mathrm{LET_\Phi}$ cf. eq. (A.4), and the Birks model, correcting the quenching with the $\mathrm{LET_\Phi}$ and not $\mathrm{LET_D}$, as such automatically incorporates the full proton LET spectrum. This is in contrast to the Chou model method (E) which relies on the variance of the LET spectrum rather than the arithmetic mean alone.

The inclusion of the secondary ions with `ExcitonQuenching` in method (B) gives a slightly better quenching correction than method (A) with primaries alone. However, the Birks model gives overall better corrections than `ExcitonQuenching`. The scintillation measurement data are shifted to match the Birks or the Chou quenching model, which furthermore are fitted directly to the data, i.e. a better fit from the Birks and Chou models are expected. As `ExcitonQuenching` relies on amorphous track structure and a kinematic model, the derived QCFs are general calculations rather than fits to the particular set of data. A drawback `ExcitonQuenching` is shown for the 81–0084 scintillator, where the method could not be applied as the light yield of the scintillator is unavailable.

4.3 Fluence thresholds for quenching

The map of the common QCF for two proton tracks separated at different distances and times in figure 3.7 shows a region where QCF > 1.056, i.e. where the excitons in the ion tracks interact significantly. The zeroth-order approximation enables an estimation of a fluence threshold for 100 MeV protons of $\Phi_{TH} = 10^{10}$ cm^{-2}, corresponding to 110 Gy, at which two proton tracks overlap sufficiently to modify the quenching. However, multiple tracks will

overlap during an irradiation (Greilich et al., 2014) and even the exciton density in the penumbras may consequently lead to substantial quenching, increasing non-linearly with the numbers of overlap. The QCF map indicates that two proton tracks should interact within 10 ns, corresponding to $\approx 3\tau$, for mutual quenching to occur. Such a pulse length is relevant for cyclotrons, where the quenching depends on the cyclotron frequency, in particular for high dose-rates. The fluence of the proton beam during the experiments was thus more than an order of magnitude smaller than Φ_{TH}, which justifies the application of the quenching models, all relying on the quenching in ion tracks being independent of each other.

5 Conclusions

The differences between the LET-averaging and the LET spectrum on the quenched luminescence signal were investigated with three quenching models and three plastic scintillators. The open-source code `ExcitonQuenching` was applied to investigate how the heavy ion fragments in the proton beam affects the quenching and hence the luminescence during proton irradiation. The `ExcitonQuenching` results show, that while the primary protons constitute 92 % to 99 % of the dose, the elevated LET of the secondary ions quenches the light emission in the secondary ion tracks more than the primary protons. Thus, the primary protons constitute more than 95 % of the luminescence signal at the entry channel and close to 100 % at the Bragg peak. The dose contribution from heavy secondary ions is too low in proton beams to require a quenching correction, but would be necessary to include for beams of heavier ions.

The quality of the five quenching correction methods were examined through χ^2/dof, accounting for the number of free model parameters. The results show that the Birks model, relying on the fluence-averaged LET, provides the best fit to the data as it includes the full proton LET spectrum due to its linearity. This is in contrast to the Chou method with an additional model parameter which depends on the both the mean and variance of the proton LET spectrum due to its non-linearity: The LET_Φ is much larger than the variance of the LET spectrum at the entry channel, and as such a good predictor for the quenching, but the large variance around the distal edge requires the inclusion of the spectrum at such a depth. The Chou model is not relevant for proton beams as its extra parameter relative to the Birks model is negligible, while the quenching correction factors are perturbed by the variance of the LET spectrum at the Bragg peak.

The volume averaging of a 1 mm diameter scintillator is numerically shown to give rise to a deviation less than 2 % for the dose and LET_Φ calculations provided the analysis is truncated at the 80 % distal dose point. The interactions between excitons from different tracks were investigated by varying both the distance between two ion tracks in an organic scintillator as well as the time between them. This led to an estimation of a fluence threshold of $10^{10}\,\mathrm{cm}^{-2}$ for pulses of the order of 10 ns, where the quenching increases greatly, and above which the Birks model no longer is applicable.

Acknowledgements

The work was supported by the Danish Cancer Society and the Danish Council for Independent Research (grant FTP, DFF – 4184-00151).

A Appendix

A.1 Amorphous track structure model

The Scholz-Kraft track structure model consists of penumbral and core radii defined as

$$r_{\max} = 0.05\,E^{1.7}\,\mu\mathrm{m}, \qquad r_{\min} = 0.01\,\mu\mathrm{m},$$

respectively, where E (MeV/nucleon) is the kinetic energy of the projectile and the radii are scaled according to the density of the medium. The model governs an initial radial exciton density n of

$$n(r) = \begin{cases} \dfrac{C}{r_{\min}^2} & \text{for} \quad r < r_{\min} \\ \dfrac{C}{r^2} & \text{for} \quad r_{\min} \le r \le r_{\max} \\ 0 & \text{for} \quad r > r_{\max} \end{cases}, \qquad \text{for} \quad C = A \cdot \mathrm{LET}\left(\pi \left[1 + 2 \ln \frac{r_{\max}}{r_{\min}}\right]\right)^{-1}, \tag{A.1}$$

where A is the light yield.

A.2 LET spectrum quenching models

Let $\varphi(s, x)$ be the intensity of the LET denoted with s at a depth x. The arithmetic mean (i.e. LET_Φ) and variance σ^2 of the spectrum at any depth is conventionally given as

$$\mathrm{LET}_\Phi(x) = \int_0^\infty s\, \varphi(s, x)\, \mathrm{d}s, \qquad \sigma^2(x) = \int_0^\infty s^2\, \varphi(s, x)\, \mathrm{d}s - \mathrm{LET}_\Phi{}^2(x), \tag{A.2}$$

respectively. Consequently, the convolution of the Chou model in eq. (2.1) and the LET spectrum as a function of depth yields a QCF as a function of depth as

$$\mathrm{QCF}(x) = \int_0^\infty \left(1 + kB \cdot s + C \cdot s^2\right) \varphi(s, x)\, \mathrm{d}s \tag{A.3a}$$

$$= 1 + kB \cdot \mathrm{LET}_\Phi(x) + C \left(\sigma^2(x) + \mathrm{LET}_\Phi{}^2(x)\right). \tag{A.3b}$$

whereas the Birks model due to its linearity is unchanged as

$$\mathrm{QCF}(x) = \int_0^\infty (1 + kB \cdot s)\ \varphi(s, x)\, \mathrm{d}s = 1 + kB \cdot \mathrm{LET}_\Phi(x). \tag{A.4}$$

A.3 Volume averaging

The dose and LET_Φ scored in volumes of different diameter in `Geant4` are shown in figure A.1. The 1 mm diameter scoring yields differences smaller than 2 % shallower than the 80 % distal dose point.

References

Agostinelli S *et al.* 2003 GEANT4 – A simulation toolkit *Nucl. Instrum. Methods* **506** 250–303

Almhagen E, Boersma DJ, Nyström H and Ahnesjö A 2018 A beam model for focused proton pencil beams *Physica Medica* **52** 27–32

Alsanea F, Therriault-Proulx F, Sawakuchi G and Beddar S 2018 A real-time method to simultaneously measure linear energy transfer and dose for proton therapy using organic scintillators *Med. Phys.* **45** 1782–9

Andersen CE 2011 Fiber-coupled Luminescence Dosimetry in Therapeutic and Diagnostic Radiology *Concepts and Trends in Medical Radiation Dosimetry* **1345** 100–19

Archambault L, Polf JC, Beaulieu L and Beddar S 2008 Characterizing the response of miniature scintillation detectors when irradiated with proton beams *Phys. Med. Biol.* **53** 1865–76

Beddar AS, Mackie TR and Attix FH 1992a Water-equivalent plastic scintillation detectors for high-energy beam dosimetry: I. Physical characteristics and theoretical considerations *Phys. Med. Biol.* **37** 1883–900

Beddar AS, Mackie TR and Attix FH 1992b Water-equivalent plastic scintillation detectors for high-energy beam dosimetry: II. Properties and measurements *Phys. Med. Biol.* **37** 1901–13

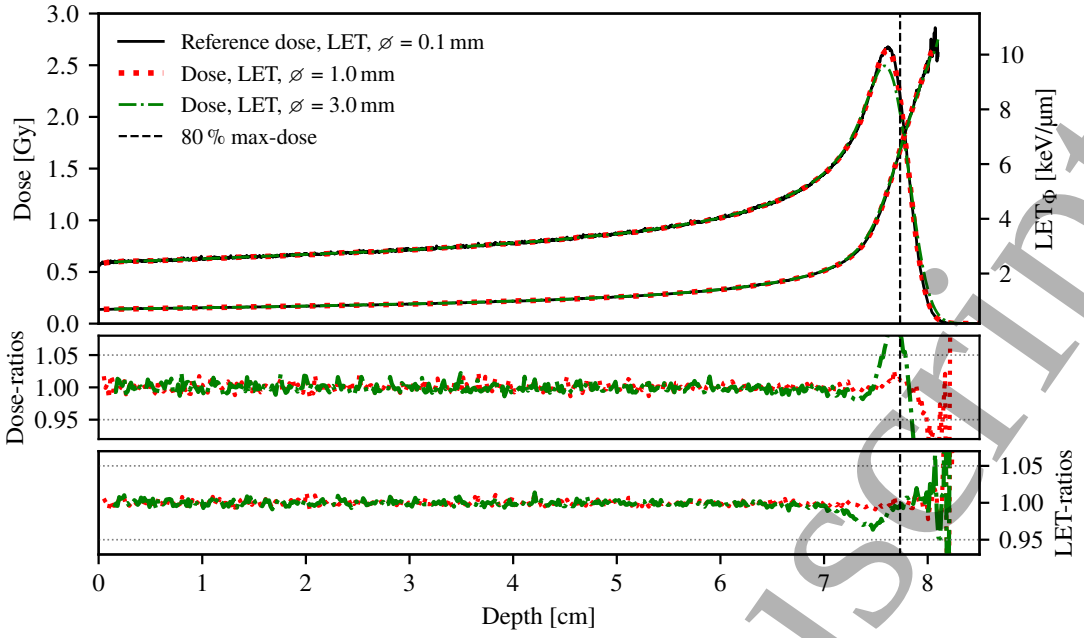

Figure A.1: `Geant4` calculations of dose and LET_Φ scored in volumes of different size. The reference dose is scored in 0.1 mm wide voxels. The ratios between the dose and LET_Φ scored in 1 mm and 3 mm diameter voxels to the reference calculations are shown in the two lower figures.

Birks JB 1951 Scintillation from organic crystals: Specific fluorescence and relative response to different radiation *Proc. Phys. Soc A* **64** 874–7

Birks JB 1964 *The Theory and Practice of Scintillation Counting: International Series of Monographs in Electronics and Instrumentation* vol 27 Elsevier

Blanc D, Cambou F and de Lafond YG 1962 Kinetics of the fast component of scintillation in a pure organic medium. Application to anthracene *C. R. l'Acad. Sci., Paris* **18** 3187–9

Blanc D, Cambou F and de Lafond YG 1964 Etude cinétique de la scintillation dans les cristaux organiques purs. *J. Physique* **25** 319–25

Boivin J, Beddar S, Bonde C, Schmidt D, Culberson W, Guillemette M and Beaulieu L 2016 A systematic characterization of the low-energy photon response of plastic scintillation detectors *Phys. Med. Biol.* **61** 5569–86

Bortfeld T 1997 An analytical approximation of the Bragg curve for therapeutic proton beams *Med. Phys.* **24** 2024–33

Chou CN 1952 The Nature of the Saturation Effect of Fluorescent Scintillators *Phys. Rev. Let.* **5** 904–5

Christensen JB and Andersen CE 2018 Relating ionization quenching in organic plastic scintillators to basic material properties by modelling excitation density transport and amorphous track structure during proton irradiation *Phys. Med. Biol.* **63** 195010

Christensen JB and Andersen CE 2019 Applications of amorphous track structure models for correction of ionization quenching in organic scintillators exposed to ion beams *Rad. Meas.* **xxx** xxx

Christensen JB, Tölli H and Bassler N 2016 A general algorithm for calculation of recombination losses in ionization chambers exposed to ion beams *Med. Phys.* **43** 5484–92

Cortés-Giraldo MA and Carabe A 2015 A critical study of different Monte Carlo scoring methods of dose average linear-energy-transfer maps calculated in voxelized geometries irradiated with clinical proton beams *Phys. Med. Biol.* **60** 2645–69

Grassberger C and Paganetti H 2011 Elevated LET components in clinical proton beams *Phys. Med. Biol.* **56** 6677–91

Greilich S, Hahn U, Kiderlen M, Andersen CE and Bassler N 2014 Efficient calculation of local dose distributions for response modeling in proton and heavier ion beams *Euro. Phys. J. D* **68** 0–4

Grün R, Friedrich T, Traneus E and Scholz M 2018 Is the dose-averaged LET a reliable predictor for the relative biological effectiveness? *Med. Phys.* **xxx** xxx

Grzanka L, Ardenfors O and Bassler N 2018 Monte Carlo simulations of spatial LET distributions in clinical proton beams *Rad. Protect. Dos.* **180** 296–9

Hoehr C, Lindsay , Beaudry J, Penner C, Strgar V, Lee R and Duzenli C 2018 Characterization of the exradin W1 plastic scintillation detector for small field applications in proton therapy *Phys. Med. Biol.* **63** 095016

Murray R and Meyer A 1961 Scintillation response of activated inorganic crystals to various charged particles *Phys. Rev.* **122** 815

Paganetti H 2002 Nuclear interactions in proton therapy : dose and relative biological effect distributions originating from primary and secondary particles *Phys. Med. Biol.* **47** 747–64

Scholz M and Kraft G 1996 Track structure and the calculation of biological effects of heavy charged particles *Adv. Space Res.* **18** 5–14

Torrisi L 2000 Plastic scintillator investigations for relative dosimetry in proton-therapy *Nucl. Instrum. Methods Phys. Res.* **170** 523–30

Wang LL, Perles LA, Archambault L, Sahoo N, Mirkovic D and Beddar S 2012 Determination of the quenching correction factors for plastic scintillation detectors in therapeutic high-energy proton beams *Phys. Med. Biol.* **57** 7767–81